Pergamon

Int. J. Heat Mass Transfer. Vol. 39, No. 14, pp. 2883–2894, 1996

0017-9310/96 $15.00+0.00

0017-9310(95)00385-1

Simulation of two-dimensional thermosolutal convection in liquid metals induced by horizontal temperature and species gradients

T. L. BERGMAN

Department of Mechanical Engineering, The University of Texas at Austin, Austin, TX 78712, U.S.A.

and

M. T. HYUN

Department of Mechanical Engineering, Cheju National University, Cheju-Do, 690-756, Korea

(*Received* 12 *June* 1995 *and in final form* 27 *October* 1995)

Abstract—Two dimensional, thermosolutal convection in molten Pb–Sn housed within a square enclosure, is simulated using a spectral method. The predictions illustrate two regimes of liquid convection which develop in response to simultaneous horizontal temperature and species concentration gradients applied to the system. Sherwood numbers for the high Schmidt number fluid are quite high, and change markedly depending upon the regime of operation. Heat transfer rates are only moderately affected by convection due to the low Prandtl number of the melt. The predictions at relatively large Rayleigh number and buoyancy ratio display highly oscillatory behavior in a manner consistent with previous experimental observations. Copyright © 1996 Elsevier Science Ltd.

INTRODUCTION

Low *Pr* thermosolutal convection occurs during solidification of metal alloys in response to (i) temperature gradients associated with cooling and (ii) species concentration gradients associated with solute rejection upon solidification. Liquid phase convection plays a primary role in determining the species and crystalline distribution within the final product [1]. Solidification simulation is motivated in large part by the difficulty of measuring velocity and concentration distributions in opaque, high temperature and potentially corrosive melts.

Although solidification simulations involving impure materials are abundant in the literature and have revealed interesting and complex behavior, little attention has been directed to accurate simulation of thermosolutal convection in low *Pr*, high *Sc* liquids. In a recent study [2], fine-scale thermosolutal behavior was noted when a spectral method was used to predict liquid phase convection in Pb–Sn and Al–Cu binary melts. In this study, single phase thermosolutal convection in Pb–Sn is simulated using a similar spectral technique. As will become evident, new and complex behavior is predicted, primarily in terms of temporal evolution of the species distributions within the liquid metal.

MATHEMATICAL MODEL

The system considered is two-dimensional (2D) thermosolutal convection of Pb–Sn in a square enclosure of characteristic dimension $2L$ (Fig. 1). The cavity's top and bottom are insulated, while the left and right faces are held at uniform cold and hot temperatures, respectively. All cavity walls are impermeable, but the left and right faces are maintained at Sn-rich (light) and Pb-rich (heavy) uniform concentrations. Hence, thermal buoyancy forces will induce counter clockwise circulation while their solutal counterparts will promote clockwise rotation. Because of the liquid's high *Sc*, large species gradients are expected to develop adjacent to the vertical walls resulting in a solutal-driven boundary layer (SDBL) flow. In contrast, the low *Pr* liquid is expected to be characterized by small temperature gradients which (since steep solutal gradients are confined to regions near the vertical walls) will produce a thermally-driven

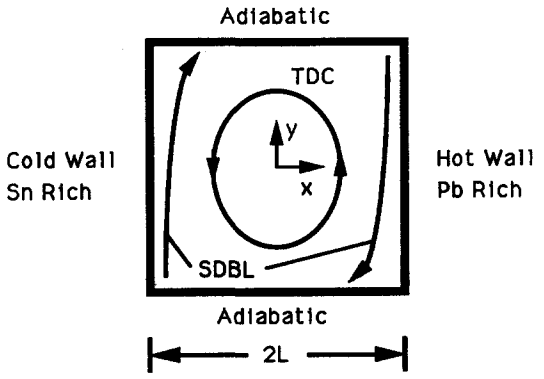

Fig. 1. Schematic of the physical system.

NOMENCLATURE

C	dimensionless concentration $= (C' - C_l)/(C_h - C_l)$
C_h	high concentration [wt%]
C_l	low concentration [wt%]
D	species diffusivity [$m^2\ s^{-1}$]
g	gravitational acceleration [$m\ s^{-2}$]
Gr_s	solutal Grashof number $= Ra \cdot N/Pr$
L	half length or height of the enclosure [m]
Le	Lewis number $= Sc/Pr$
n	number of spatial modes
N	buoyancy ratio $= \beta_C \cdot (C_h - C_l)/\beta_T \cdot (T_h - T_c)$
$\overline{Nu}$	mean Nusselt number $= \int_{-1}^{1} (\partial T(t, -1, y)/\partial x) dy$
p	pressure [$N\ m^{-2}$]
Pr	Prandtl number, ν/α
Ra	Rayleigh number $= g\beta_T(T_h - T_c) \cdot (2L)^3/(\nu \cdot \alpha)$
Sc	Schmidt number $= \nu/D$
$\overline{Sh}$	mean Sherwood number $= \int_{-1}^{1} (\partial C(t, -1, y)/\partial x) dy$
T	dimensionless temperature $= (T' - T_c)/(T_h - T_c)$
T_c	cold wall temperature [°C]
T_h	hot wall temperature[°C]
t	dimensionless time $= t'\nu/L^2$
u	dimensionless x-direction velocity $= u'L/\nu$
v	dimensionless y-direction velocity $= v'L/\nu$
x	dimensionless horizontal coordinate $= x'/L$
y	dimensionless vertical coordinate $= y'/L$.

Greek symbols

α	thermal diffusivity [$m^2\ s^{-1}$]
β_C	coefficient of solutal expansion $= \rho^{-1}(\partial\rho/\partial C)_{T,p}$
β_T	coefficient of thermal expansion $= \rho^{-1}(\partial\rho/\partial T)_{C,p}$
ε	$\overline{Sh}$ error
ν	kinematic viscosity [$m^2\ s^{-1}$]
ρ	mass density [$kg\ m^{-3}$]
ψ	dimensionless stream function $= \psi'/\nu$
ω	dimensionless vorticity $= \omega' L^2/\nu$.

Subscripts and superscript

max	maximum
min	minimum
′	dimensionless value.

core (TDC). Similar behavior has been noted in experiments involving transparent, moderate Pr (and high Le) liquids [3, 4].

In this study, the melt is considered to be an opaque, Boussinesq liquid undergoing two-dimensional flow. The governing equations are written in terms of vorticity–velocity functions (with the origin at the center of the cavity) as follows.

$$\partial^2 v/\partial x^2 + \partial^2 v/\partial y^2 = \partial\omega/\partial x \quad (1)$$

$$\partial^2 u/\partial x^2 + \partial^2 u/\partial y^2 = -\partial\omega/\partial y \quad (2)$$

$$8 \cdot Pr \cdot ((\partial\omega/\partial t + u \cdot \partial\omega/\partial x + v \cdot \partial\omega/\partial y) - (\partial^2\omega/\partial x^2 + \partial^2\omega/\partial y^2)) = Ra \cdot (\partial T/\partial x - N \cdot \partial C/\partial x) \quad (3)$$

$$Pr \cdot (\partial T/\partial t + u \cdot \partial T/\partial x + v \cdot \partial T/\partial y) = \partial^2 T/\partial x^2 + \partial^2 T/\partial y^2 \quad (4)$$

$$Sc \cdot (\partial C/\partial t + u \cdot \partial C/\partial x + v \cdot \partial C/\partial y) = \partial^2 C/\partial x^2 + \partial^2 C/\partial y^2. \quad (5)$$

Although diffusion-induced velocities will exist at $x = \pm 1$, they are expected to be small relative to characteristic velocities within the liquid. The liquid is initially at a uniform species concentration midway between the applied wall concentrations, and the initial temperature distribution is linear, approximating conditions which are expected to exist prior to the onset of anti-symmetric fluid motion in a low Pr, high Sc liquid subject to horizontal species concentration and temperature gradients. Hence, the boundary and initial conditions are:

$$u(t, \pm 1, y) = u(t, x, \pm 1) = v(t, \pm 1, y) = v(t, x, \pm 1) = 0 \quad (6a)$$

$$T(t, -1, y) = 0, \quad T(t, 1, y) = 1, \quad \partial T(t, x, \pm 1)/\partial y = 0 \quad (6b)$$

$$C(t, -1, y) = 1, \quad C(t, 1, y) = 0, \quad \partial C(t, x, \pm 1)/\partial y = 0 \quad (6c)$$

$$u(0, x, y) = v(0, x, y) = 0, \quad T(0, x, y) = 0.5x + 0.5, \quad C(0, x, y) = 0.5. \quad (6d)$$

Equations (1)–(5) were solved using a Chebyshev collocation (spectral) technique [5]. In short, the dependent variable spatial distributions are expanded in doubly truncated series of Chebyshev polynomials, utilizing the usual Chebyshev–Gauss–Lobatto quadrature points [6]. Time integration is via a finite-difference technique employing the semi-implicit Adams–Bashforth/second-order backward Euler procedure. When applied to the transport equations (3)–

(5), this procedure results in 2D Helmholtz equation at each time level. A full matrix diagonalization algorithm [5] is used to solve the Helmholtz and Poisson equations (1) and (2). A key feature of the numerical scheme is the use of an influence matrix technique to obtain proper vorticity boundary conditions. In the vorticity–velocity formulation, the kinematic definition of boundary vorticity is enforced to construct the influence matrix.

Details of the influence matrix technique, along with an outline of the general numerical procedure are discussed elsewhere [7] and will not be repeated here. The algorithm performance and accuracy have been assessed, and predictions for natural convection in air are spectrally convergent [7]. The algorithm has been applied successfully to thermosolutal convection problems, and the performance of this spectral technique relative to that of the finite volume method has been documented [8]. The predictions are considered to be space and time step resolution independent, as discussed in the Appendix. Spatial resolutions ranged from 65×65 to 177×177 modes, while time steps were varied from 10^{-5} to 1.25×10^{-6} (with finer space and time resolution at higher Ra and N). The predictions reported here required approximately one year of CPU time on an IBM RS 6000 Model 350 workstation with 128 MByte RAM. The simulation of the extreme $Ra \cdot N$ case required approximately 4 months of CPU time and 50 MByte RAM.

RESULTS

Although there is uncertainty regarding properties of molten Pb–Sn, they were taken to be $Pr = 0.02$ and $Sc = 150$ ($Le = 7500$). Note that the value of N based upon the slope of the liquidus (dC/dT) of Pb-rich, Pb–Sn solutions ($N \equiv -(\beta_C/\beta_T) \cdot (dC/dT)$) is approximately -10, and this buoyancy ratio may develop during solidification of an initially uniform concentration binary melt [9].

Selected concentration, stream function and temperature distributions for the $Ra = 100$, $N = -10$ case are shown in Fig. 2. Twenty concentration and temperature contours (evenly spaced) are shown, while 10 negative (counter clockwise) stream function contours (including ψ_{min} and 0) are included. Positive (clockwise) stream function values are listed in the figure caption.

Because of the high Sc and low Pr characterizing the liquid, fine, moderate and coarse structure is associated with the predicted concentration, stream function and temperature distributions. As expected, solutal boundary layers develop along the vertical walls and co-exist with a thermally driven core. With time, the heavy, Pb-rich liquid fills the bottom of the cavity (the lighter, Sn-rich liquid rises) and, eventually ($t \approx 3.15$), solutal stratification develops throughout the enclosure. Solutal buoyancy forces, acting in conjunction with low species diffusivity rates, shrink the central rotating core. Because of the liquid's low Pr, heat transfer is conduction dominated and $\overline{Nu}$ values are very small (near unity). Mass transfer rates will be quantified and discussed later.

Figure 3 includes predicted concentration, stream function and temperature distributions for the $Ra = 5000$, $N = -10$ case. As in Fig. 2, 20 evenly spaced concentration and temperature contours are shown, while 10 negative stream function contours are included. A range of scales is again noted, with the finest ones associated with the concentration distribution. As noted in the previous figure, a Pb-rich SDBL develops along the hot (right) wall and, as evident in the bottom right corner, begins to fill the bottom of the enclosure with Pb-rich liquid. In contrast to the $Ra = 100$ case, however, Pb-rich liquid is torn from the SDBL at approximately cavity mid-height and is subsequently blended into the interior regions of the domain. The entrainment is driven by the counter clockwise rotation in the TDC, with a stagnation region persisting at approximately cavity mid-height. Once incorporated into the core, the liquid retains its species identity with remarkable tenacity, as expected due to its high Sc. The low Pr liquid's temperature distribution is only moderately affected by advection and is still uninteresting. $\overline{Nu}$ values are small (approx 1.5) and mass transfer rates will be discussed later.

Because of the vigor with which individual entrained "droplets" retain their solutal identity, interpretation of the system response is difficult if $0 \leqslant C \leqslant 1$ is plotted (as in Fig. 3). Figure 4 includes a series of evenly-spaced snapshots ($\Delta C = 0.05$) of concentration contours for $0.0 \leqslant C \leqslant 0.45$ (Pb-rich) liquid over the time interval ($0.1825 \leqslant t \leqslant 0.21$). Individual droplets are targeted in the figure.

Close inspection of Fig. 4 shows that drops are, in general, formed from the tips of Pb-rich fingers which are thermally torn from the SDBL. Droplet formation is intermittent and complex [droplet 2, Figs. 4(a)–(e)] and seems to be affected by proximity to the enclosure ceiling. Different size drops are generated (compare droplets 2, 3 and 4), they can undergo stretching and folding [droplet 1, Figs. 4(b)–(e)], and can break with subsequent bifurcating trajectories [droplets 2a and 2b, Figs. 4(h)–(k)]. The potential impact of the fine scale species fragmentation (when viewed in conjunction with the remarkably *inactive* temperature distributions such as shown in Fig. 3) on homogeneous solidification dynamics has been discussed at some length [8]. In short, fine Pb–Sn drops can cool below their liquidus temperature as they are advected into cold liquid regions, possibly leading to equi-axed solidification within the melt.

The flow field associated with Fig. 4 is shown in Fig. 5. Here, negative stream function contours are shown at increments of $\Delta\psi = 10$, positive contours are shown in increments of $\Delta\psi = 1$, and values of ψ_{min} and ψ_{max} are listed in the figure caption. Intermittent recirculation is noted in the upper right (and lower

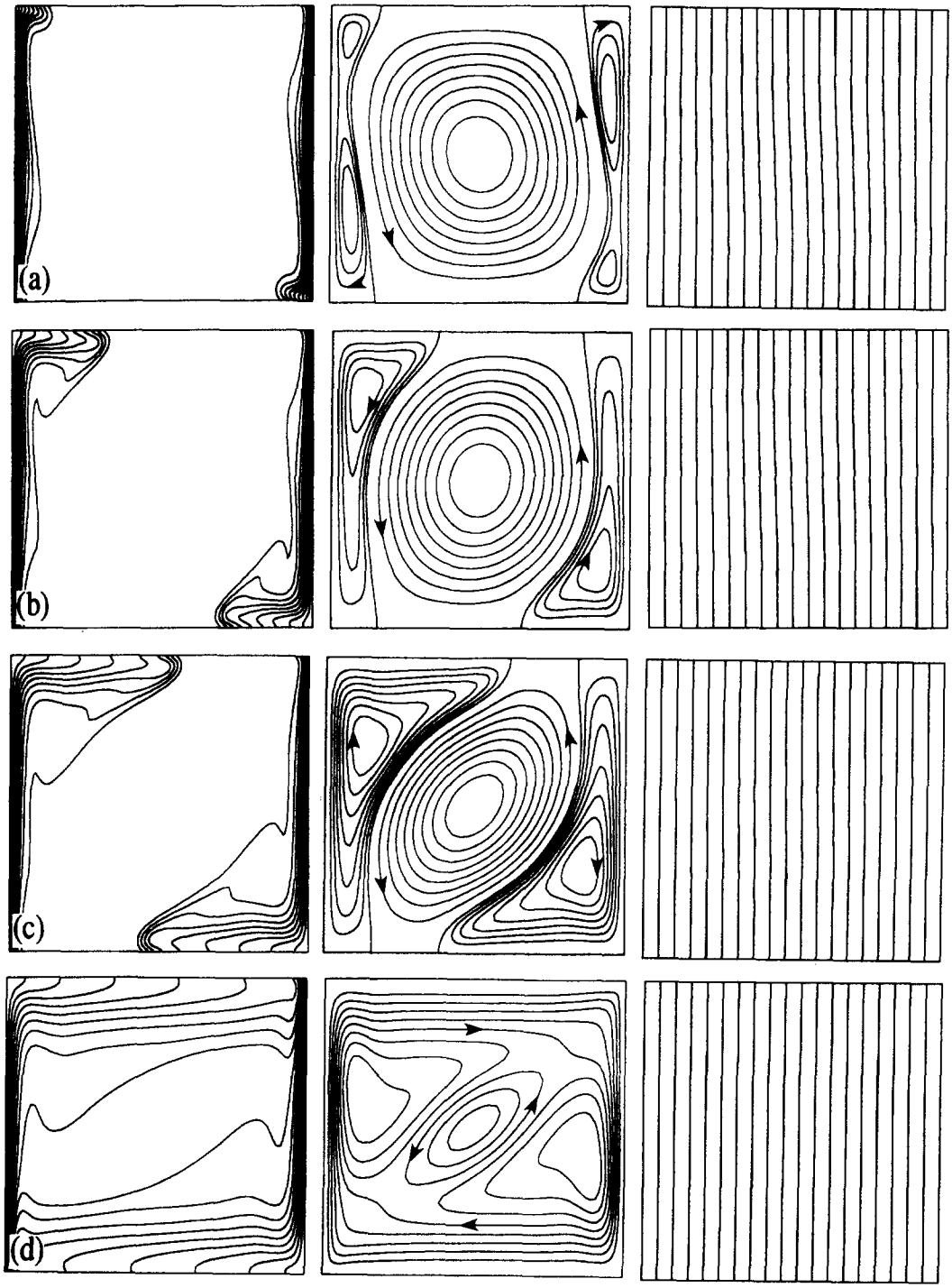

Fig. 2. Predicted concentration, stream function and temperature distributions for $Ra = 100$, $N = -10$ at: (a) $t = 0.3$ ($\psi_{min} = -4.94$, $\psi_{max} = 0.189$, $\psi = 0.047$, 0.095, 0.142); (b) $t = 0.75$ ($\psi_{min} = -3.895$, $\psi_{max} = 0.385$, $\psi = 0.077$, 0.154, 0.231, 0.308; (c) $t = 1.35$ ($\psi_{min} = -1.883$, $\psi_{max} = 0.466$, $\psi = 0.058$, 0.117, 0.175, 0.233, 0.291, 0.350, 0.408) and (d) $t = 3.15$, ($\psi_{min} = -0.321$, $\psi_{max} = 0$).

left) corner of the cavity [Figs. 5(c) and (i)] and coincides with droplet formation [Figs. 4(c) and (i)]. The position of the wall stagnation is remarkably steady and consistent with that of Fig. 3. Circulation with the Pb-rich liquid filling the cavity bottom (lower right corner of Fig. 4) is weak, but can be induced when the region is grazed by heavy droplets which are thermally advected around the core [Figs. 4(d) and 5(d), as well as Figs. 4(h) and 5(h)]. Obviously, the side wall mass transfer rates will be affected by the

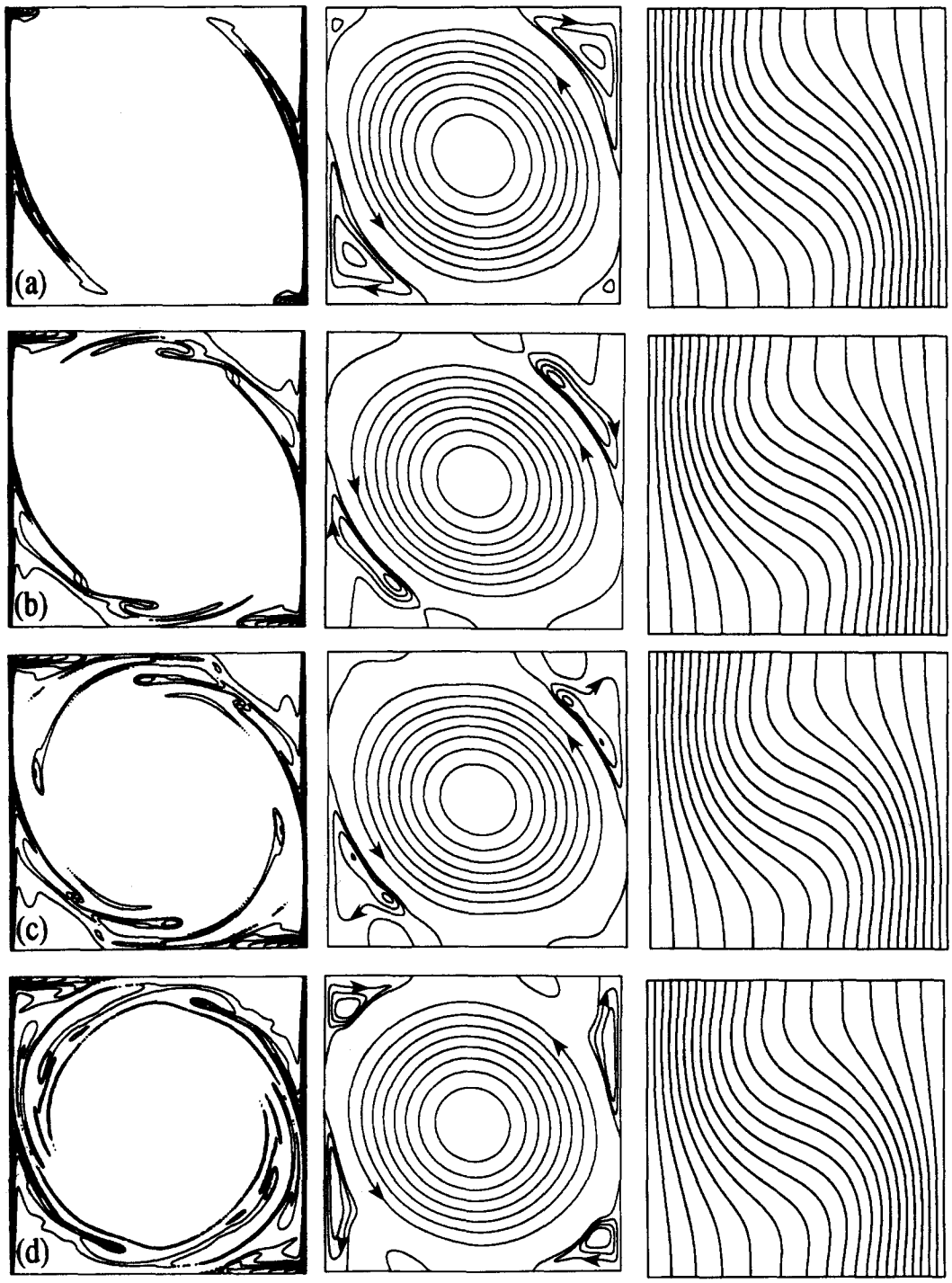

Fig. 3. Predicted concentration, stream function and temperature distributions for $Ra = 5000$, $N = -10$ at: (a) $t = 0.06$ ($\psi_{min} = -124.3$, $\psi_{max} = 0.97$, $\psi = 0.3, 0.6, 0.9$); (b) $t = 0.14$ ($\psi_{min} = -141.7$, $\psi_{max} = 2.1$, $\psi = 0.6, 1.2, 1.8$); (c) $t = 0.17$ ($\psi_{min} = -144.7$, $\psi_{max} = 1.6$, $\psi = 0.5, 1.0, 1.5$) and (d) $t = 0.22$ ($\psi_{min} = -152.2$, $\psi_{max} = 0.89$, $\psi = 0.2, 0.4, 0.6$).

thermosolutal convection illustrated in Figs. 4 and 5, but heat transfer rates are not altered significantly because of the extreme Le values of the metal.

Mass transfer rates

Spatially-averaged mass transfer rates (at the cold wall) are shown in Fig. 6. For all cases, $\overline{Sh}$ is initially infinite and, as species diffuse towards $x = 0$, solutal

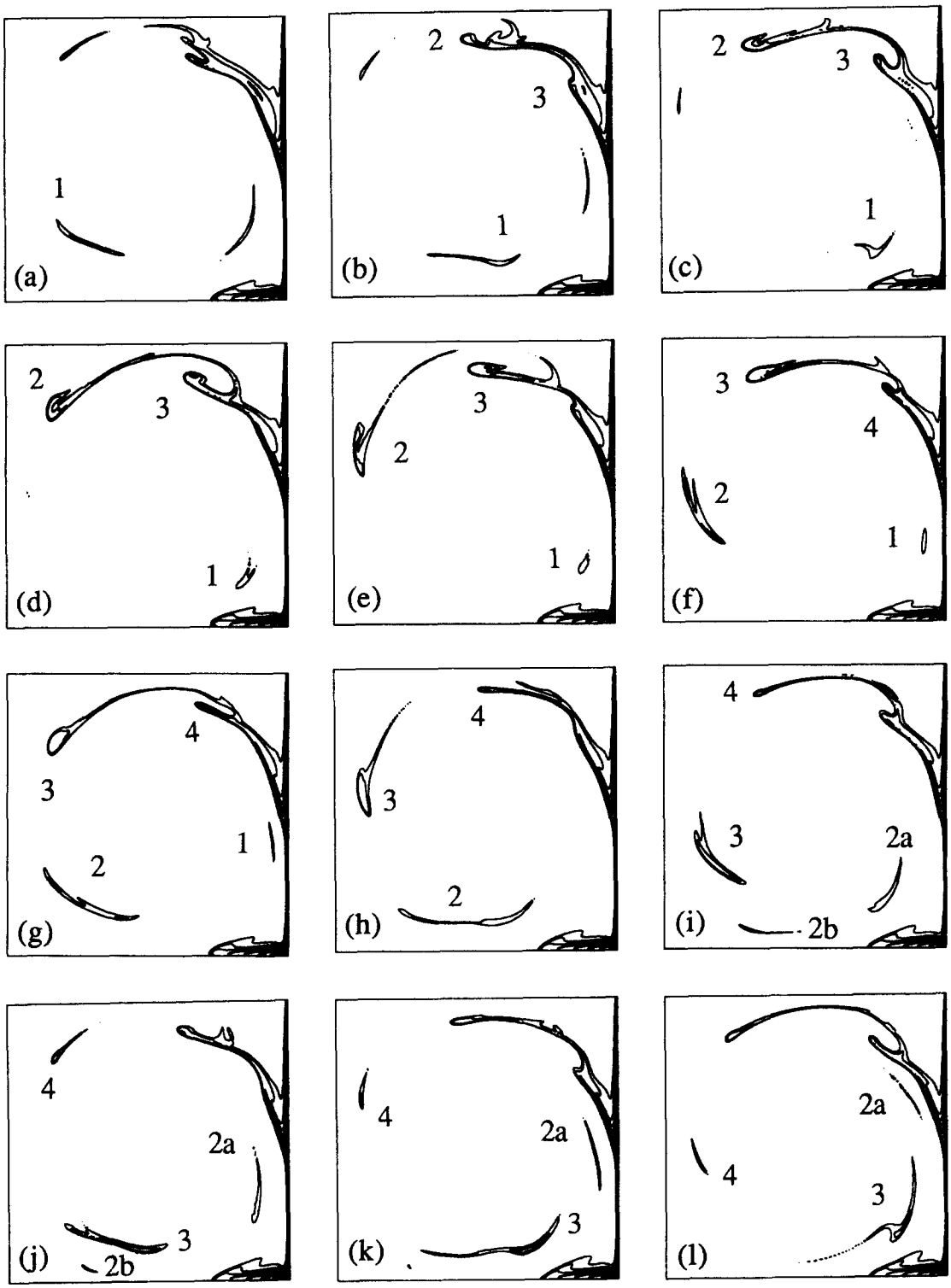

Fig. 4. Time series of Pb-rich concentrations. The initial time shown is $t = 0.1825$ and results are shown in increments of $\Delta t = 0.0025$. Contour values ($C \leqslant 0.45$) are shown at increments of $\Delta C = 0.05$.

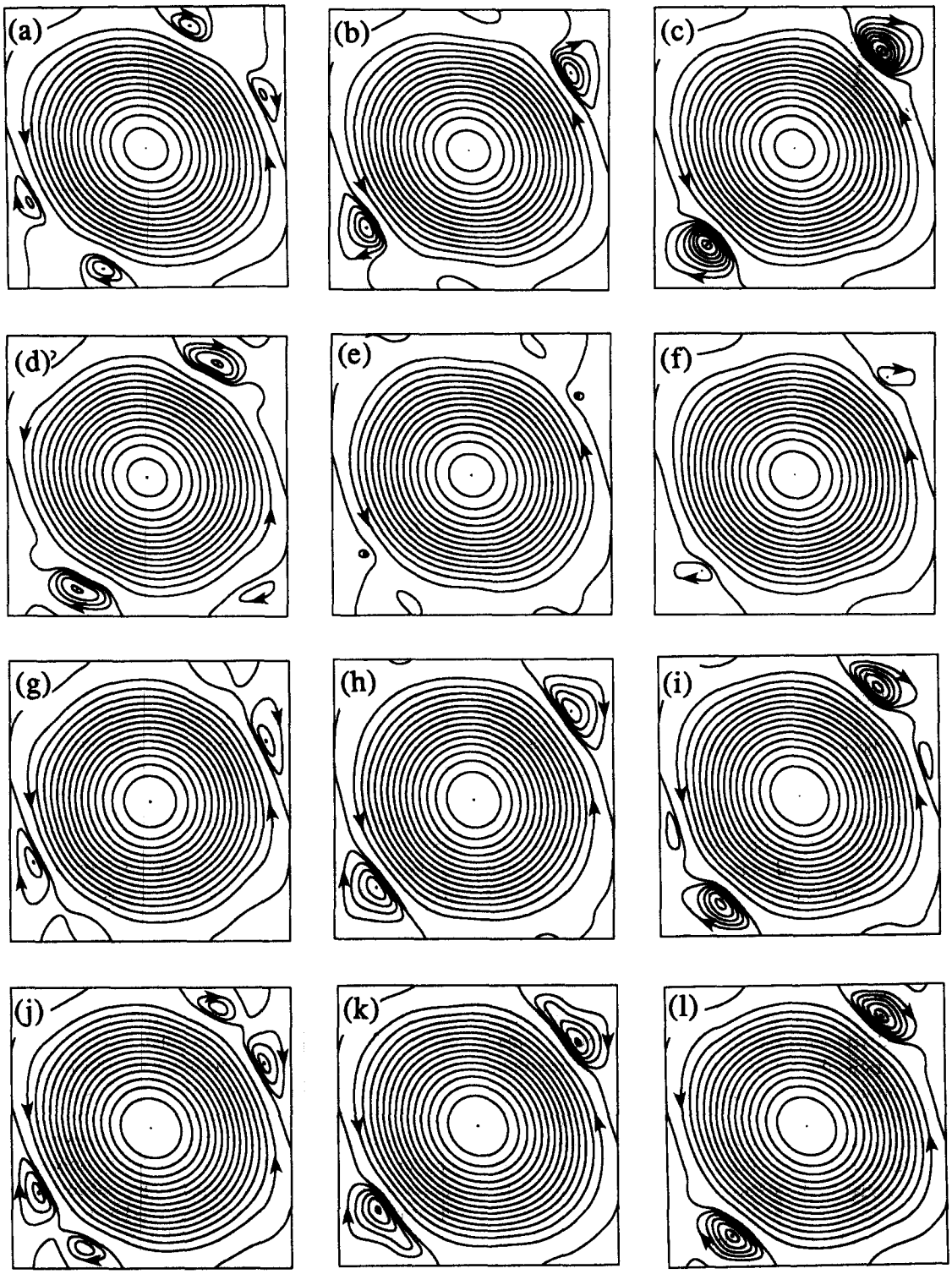

Fig. 5. Stream function time series corresponding to Fig. 4. Values of ψ_{min} (ψ_{max}) are: (a) −146.3 (2.76); (b) −146.1 (4.96); (c) −145.2 (7.25); (d) −145.2 (4.11); (e) −146.6 (1.06); (f) −148.0 (1.59); (g) −149.2 (2.44); (h) −150.4 (4.82); (i) −151.6 (5.24); (j) −152.4 (3.39); (k) −152.29 (5.09) and (l) −151.6 (5.32).

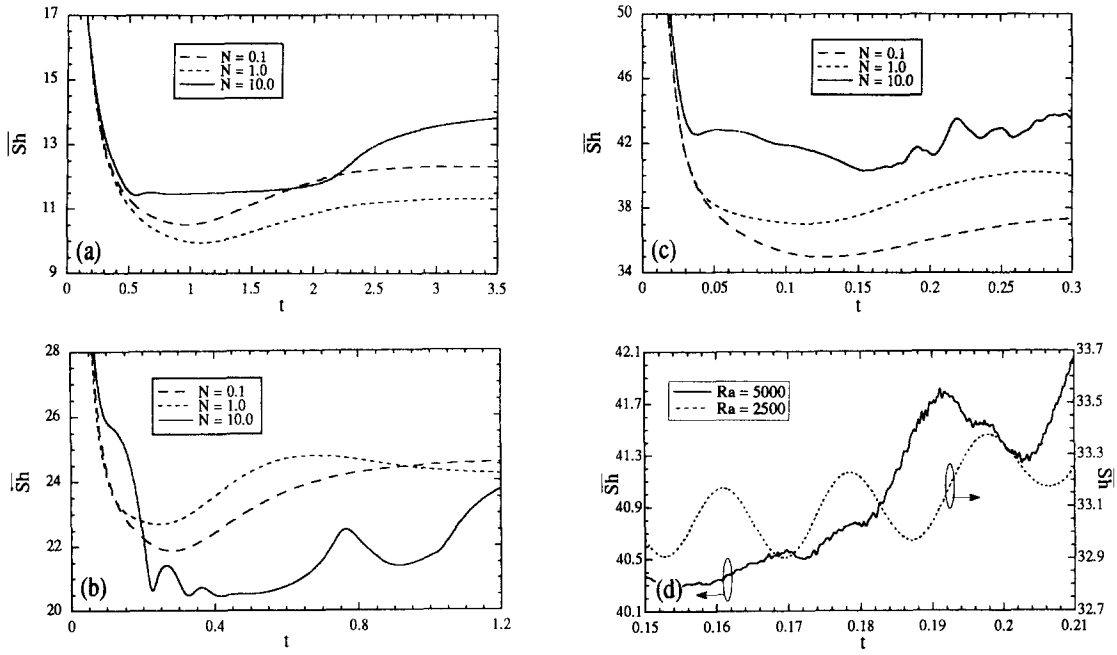

Fig. 6. Average mass transfer rates for: (a) $Ra = 100$; (b) $Ra = 1000$; (c) $Ra = 5000$ and (d)$Gr_s^{1/4} \approx 40$.

buoyancy forces become sufficient to establish the SDBL (at, for example, $t \approx 0.5$ for the $Ra = 100$ cases).

For the $Ra = 100$ cases [Fig. 6(a)] the $\overline{Sh}$ histories approach steady state for $N = -0.1$ and -1 cases, with $\overline{Sh}$ decreasing, and then increasing with larger solutal buoyancy forces. Predicted stream function and concentration distributions for the $Ra = 100$, $N = -0.1$, -1 and -10 cases at $t = 3.15$ are shown in Fig. 7 (the temperature distribution is conduction dominated and, as such, is not shown). In this Ra–N regime, solutal buoyancy forces are too weak to drive significant clockwise motion (at $N = -0.1$ and -1) until, as N becomes sufficiently large (-10), "filling box" behavior occurs. Without significant solutally-induced recirculation, $\overline{Sh}$ values are relatively small and, presumably, critical N values exist where solutal and thermal buoyancy figures offset (at $N \approx -1$) for which $\overline{Sh}$ is minimized. It is noted that the predicted stream function and concentration distributions for the $Ra = 100$, $N = -0.1$ and -1 cases at $t \approx 1.5$ are very similar to those shown in Fig. 7, and $\overline{Nu} \approx 1$ for all N cases.

Similar overall species transport rates are noted for the $Ra = 5000$ case [Fig. 6(c)] in the sense that $\overline{Sh}$ is maximized for the $N = -10$ scenario. Representative predicted stream function and concentration distributions for the $Ra = 5000$, $N = -0.1$, -1 and -10 cases are shown in Fig. 8 at $t = 0.18$. In this Ra–N regime, significant filling box behavior is not evident for any N value (although it may become pronounced at later times). Rather, mass transfer augmentation for the $N = -10$ situation is due to enhanced mixing associated with the intermittent entrainment phenomena previously discussed. In contrast to the $Ra = 100$ results, solutal buoyancy forces are sufficient to promote small SDBL activity in the upper right and lower left corners of the enclosure at $N = -1$, which, in turn, increases $\overline{Sh}$ values relative to the $N = -0.1$ case.

Transitional behavior (in terms of *minimum* $\overline{Sh}$ occuring at $N = -10$) is noted for the $Ra = 1000$ situation [Fig. 6(b)]. This transitional mode can be explained by considering the representative stream function and concentration distributions of Fig. 9. In the $N = -10$ case [Fig. 9(c)], the thermal and solutal buoyancy forces combine to produce small liquid velocities. Large, nearly stagnant fluid regions line the vertical enclosure walls, reducing mass transfer rates. (Similar stagnation regions exist for $0.3 \leqslant t \leqslant 1.2$.) Minimum counter clockwise stream function values are decreased by an order of magnitude relative to the smaller N cases. For $N = -1$ [Fig. 9(b)], only slight recirculations exist in the upper right and lower left cavity corners, while the recirculations located in these positions for the $N = -0.1$ case [Fig. 9(a)] only modestly affect the species distributions.

As previously noted, the fine scale solutal structure and wall stagnation regions of the $Ra = 5000$, $N = -10$ case are remarkably consistent with the experimental observations of Jiang *et al.* [3, 4] who examined thermosolutal cavity convection in a transparent, moderate Pr liquid. Fig. 6(d) shows part of the $\overline{Sh}$ histories for the $Ra = 5000$, $N = -10$ case,

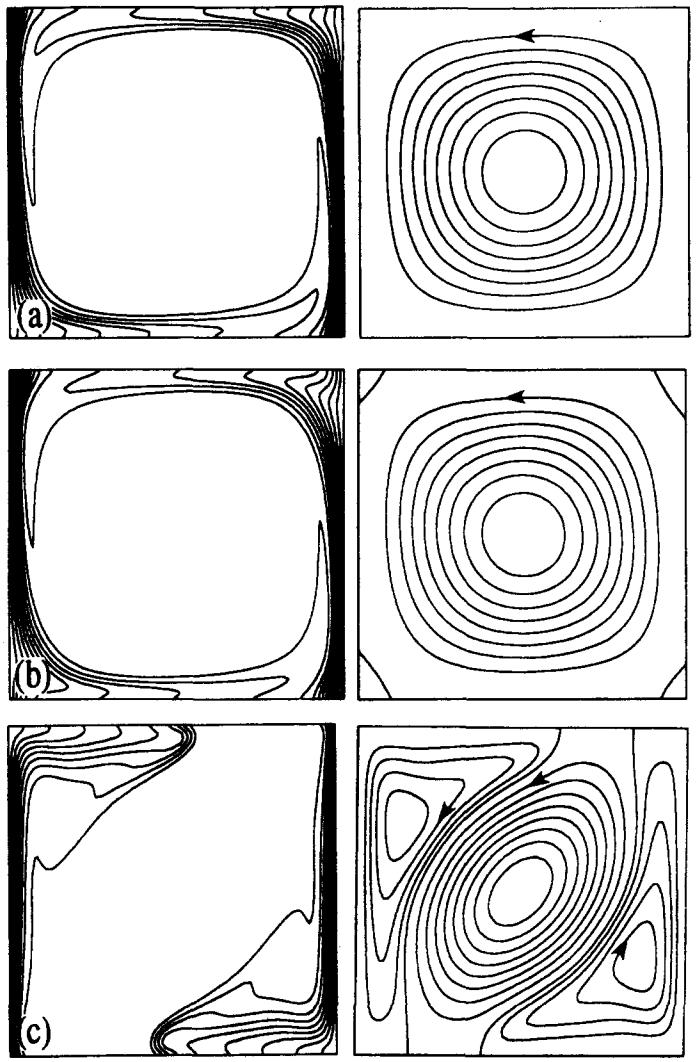

Fig. 7. Species concentration (left) and stream function (right) distributions for $Ra = 100$. Results are shown at $t = 3.15$ for: (a) $N = -0.1$, $\psi_{min} = -6.305$, $\psi_{max} = 0$; (b) $N = -1$, $\psi_{min} = -6.20$, $\psi_{max} = 0.003$ and (c) $N = -10$, $\psi_{min} = -1.883$, $\psi_{max} = 0.466$, $\psi = 0.1, 0.2, 0.3$ and 0.4.

along with a second prediction associated with $Ra = 2500$, $N = -20$. The $Ra = 5000$, $N = -10$ predictions clearly show high frequency mass transfer rates (which are independent of the time step, as shown in the Appendix).

When viewed in conjunction with Figs. 4 and 5, it is interesting to note that $\overline{Sh}$ generally increases with growing corner activity [$0.1825 \leqslant t \leqslant 0.19$, Figs. 5(a)–(d); $0.225 \leqslant t \leqslant 0.21$, Figs. 5(h)–(l)] and decreases with corner stagnation [$0.19 \leqslant t \leqslant 0.2$, Figs. 5(b)–(g)]. Alternatively, it is noted that maximum mass transfer rates occur when droplets complete a rotation about the cavity and impinge upon the cold wall SDBL [$t = 0.19$ and 0.21, Figs. 4(d) and (l)]. The relationship between SDBL impingement and promotion of maximum $\overline{Sh}$ is, however, not direct since minimum $\overline{Sh}$ ($t \approx 0.225$) also occurs during SDBL bombardment [Fig. 4(i)].

Finally, as evident in Fig. 6(d), the $Ra = 2500$, $N = -20$ $\overline{Sh}$ behavior is characterized by low frequency fluctuation. It is interesting to note that both predictions shown in Fig. 6(d) are associated with $Gr_s^{1/4} \approx 40$, and experimental measurements of fluctuating $\overline{Sh}$ have been made in this extremely high Gr_s range using a $Pr = 7$. $Sc = 2900$ liquid (Fig. 2 of [4]). It is remarkable (and perhaps fortuitous since a very different liquid was used) that (with modest extrapolation to $Gr_s^{1/4} = 40$) the experimental results (Fig. 6 of [4]) show a similar transition in mass transfer from low to high frequency behavior as N is reduced from -20 to ≈ -10. The highest frequency behavior is attributed to the TDC–SDBL interaction discussed

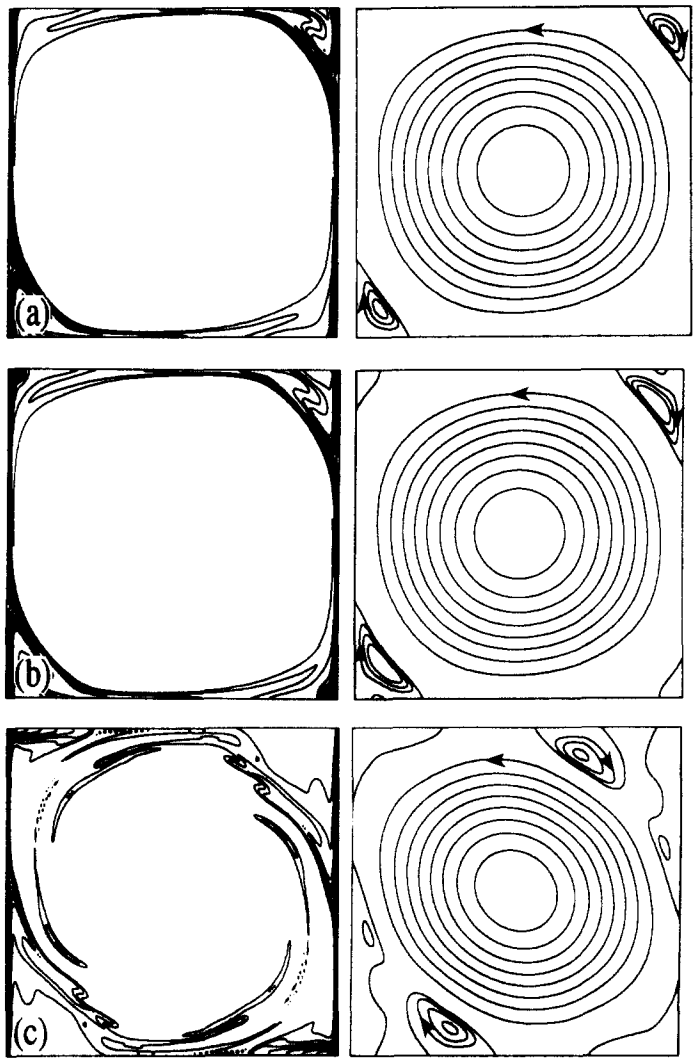

Fig. 8. Species concentration (left) and stream function (right) distributions for $Ra = 5000$. Results are shown at $t = 0.18$ for: (a) $N = -0.1$, $\psi_{min} = -170$, $\psi_{max} = 0.249$, $\psi = 0.07, 0.14, 0.21$; (b) $N = -1$, $\psi_{min} = -170$, $\psi_{max} = 0.44$, $\psi = 0.1, 0.2, 0.3$ and (c) $N = -10$, $\psi_{min} = -146.2$, $\psi_{max} = 3.26$, $\psi = 1.0, 2.0, 3.0$.

previously. A similar TDC–SDBL interaction phenomenon was used to explain the experimental results [3, 4].

SUMMARY

In this study, thermosolutal convection in a low *Pr*, high *Sc* liquid metal was simulated. The predicted system response illustrates two distinct regimes of behavior in which large solutal buoyancy forces lead to enhanced mass transfer rates. The regimes are separated by a transition region where thermal and solutal buoyancy forces can become balanced, resulting in a velocity reduction throughout the cavity and, in turn, small mass transfer rates. At high *Ra* and *N*, fragmentation of the species concentration distribution occurs, associated with a complex and highly time-dependent droplet formation process. Perhaps fortuitously, the predictions indicate rapidly fluctuating transport rates in the same regions of operation as those measured in independent experimental studies involving very different (modest *Pr*, high *Sc*) liquids.

Although insight into thermosolutal phenomena in high *Le*, low *Pr* liquids has been gained, it is unknown whether the predicted behavior is indeed two-dimensional. Three-dimensionality is common in thermosolutal systems, and is likely when fragmentation of the species distribution is induced. Unfortunately, only local temperatures can be measured relatively easily in liquid metals, and, as implied here, the measured temperatures cannot unveil the rich complexity of the species distributions (and to a lesser extent, the

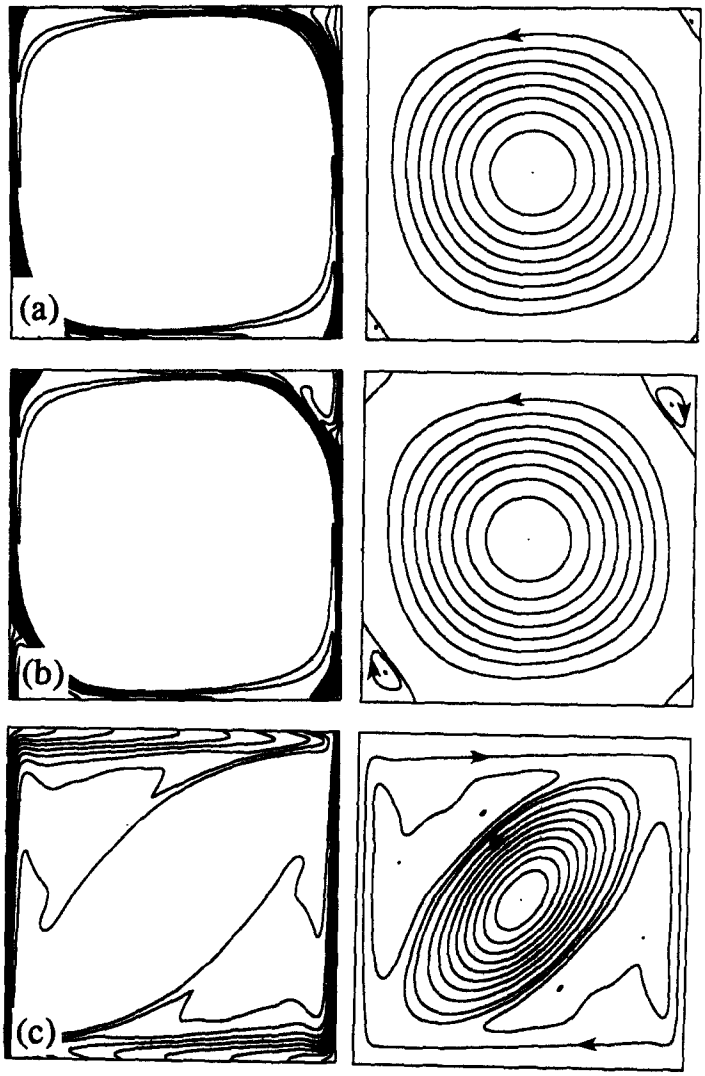

Fig. 9. Species concentration (left) and stream function (right) distributions for $Ra = 1000$. Results are shown at $t = 1.0$ for: (a) $N = -0.1$, $\psi_{min} = -57.02$, $\psi_{max} = 0.0016$; (b) $\psi_{min} = -56.66$, $\psi_{max} = 0.152$, $\psi = 0.077$ and (c) $\psi_{min} = -5.99$, $\psi_{max} = 0.97$, $\psi = 0.32, 0.65$.

velocity distributions) which may develop during, for example, metallic alloy solidification. Recourse to direct 3D simulation may be needed, but this will be an extremely expensive approach.

Acknowledgement—The second author would like to thank the Korea Science and Engineering Foundation for financial assistance.

REFERENCES

1. C. Beckermann and R. Viskanta, Mathematical modeling of transport phenomena during alloy solidification. *Appl. Mech. Rev.* **46**, 1–27 (1993).
2. M. T. Hyun, D. C. Kuo, T. L. Bergman and K. S. Ball, Direct simulation of double diffusion in low *Pr* liquids, *Numer. Heat Transfer* **27**, 639–650 (1995).
3. H. D. Jiang, S. Ostrach and Y. Kamotani, Thermosolutal convection flow regimes with opposed buoyancy forces in shallow enclosures, *Phys. Chem. Hydrodyn.* **10**, 599–613 (1988).
4. H. D. Jiang, S. Ostrach and Y. Kamotani, Unsteady thermosolutal transport phenomena due to opposed buoyancy forces in shallow enclosures. *J. Heat Transfer*, **113**, 135–140 (1991).
5. U. Ehrnstein and R. Preyet, A Chebyshev collocation method for the Navier–Stokes equations with application to double-diffusive convection, *Int. J. Numer. Meth. Fluids*, **9**, 427–452 (1989).
6. C. Canuto, M. Y. Hussaini, A. Quateroni and T. A. Zang, *Spectral Methods in Fluid Dynamics*. Springer, New York (1988).
7. K. S. Ball and D. C. Kuo, Spectral simulation of thermal convection using a vorticity–velocity formulation, *Proceedings of the 10th International Heat Transfer Confer-*

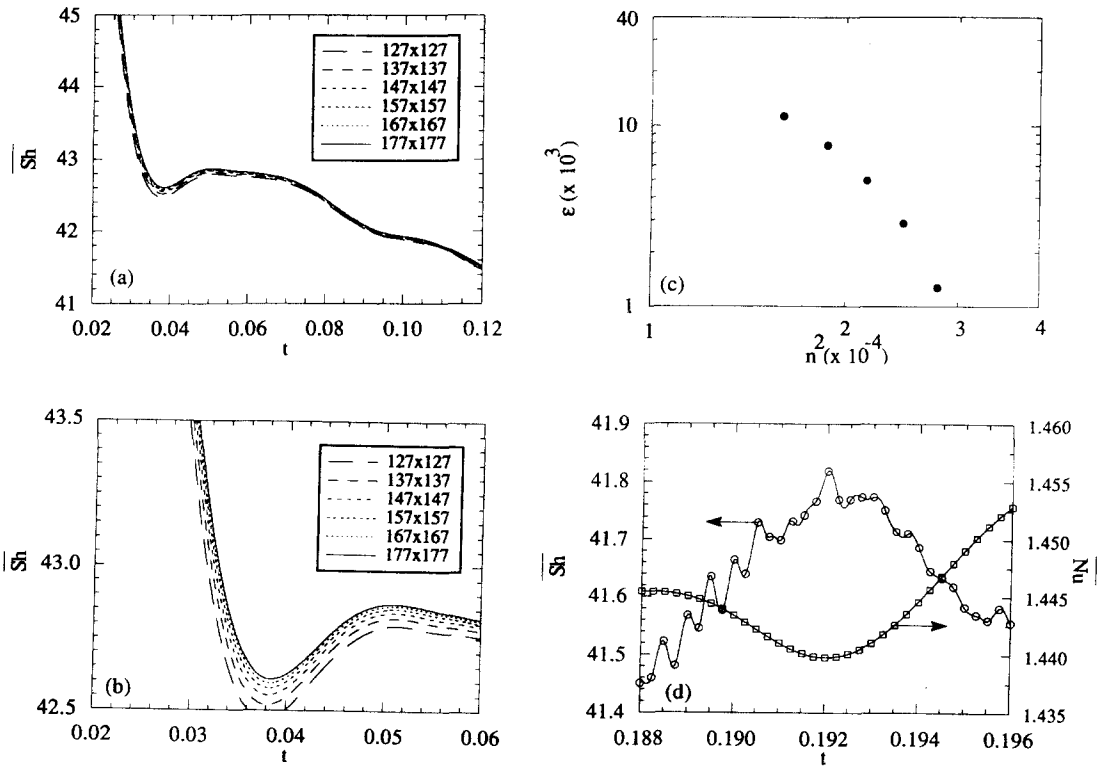

Fig. A1. Spatial and temporal resolution showing (a) average species transfer rates for different spatial resolutions, (b) detailed species transfer rates at the onset of solutally driven convection, (c) spectral convergence and (d) time step dependence of heat and mass transfer rates.

ence, Vol. 7, pp. 313–318. Institution of Chemical Engineers, Rugby, Warwickshire (1994).

8. M. T. Hyun, D. C. Kuo, T. L. Bergman and K. S. Ball, Simulation of thermosolutal convection in Pb–Sn: FVM and spectral predictions, *Proceeding of the 30th 1995 National Heat Transfer Conference*, Vol. 4, pp. 63–69, ASME, New York (1995).
9. P. J. Prescott and F. P. Incropera, Numerical simulation of a solidifying Pb–Sn alloy: the effects of cooling rate on thermosolutal convection and macrosegregation, *Metall. Trans*, **22B**, 529–540 (1991).

APPENDIX

Simulations were performed with increasing spatial and temporal resolution until changes in the predicted mass transfer rates became arbitrarily small. To illustrate, instantaneous $\overline{Sh}$ histories are shown for the $Ra = 5000$, $N = -10$ case (for $t \leqslant 0.12$) in Figs. A1 (a) and (b) using a time step of 2.5×10^{-6}. As evident, the $\overline{Sh}$ behavior is similar for all spatial resolutions, and the onset of convection occurs at nearly the same time regardless of the spatial resolution [Fig. A1 (b)]. A measure of the convergence can be made by comparing the predicted mass transfer rates and is

$$\varepsilon = \frac{1}{t^*}\int_0^{t^*} \frac{|\overline{Sh}(t)_n - \overline{Sh}(t)_{n=177}|}{\overline{Sh}(t)_{n=177}}\,\mathrm{d}t$$

where $t^* = 0.12$. Figure A1 (c) shows the sensitivity of ε to the spatial resolution, and spectral convergence is noted. Predicted concentration distributions at $t = 0.14$ for the $Ra = 5000$, $N = -10$ case are shown for various spatial resolutions in [8]. Qualitative differences in the predicted concentration distributions cannot be noted for predictions with spatial resolution greater than 147×147.

Time step dependence information is shown in Fig. A1 (d) for the $Ra = 5000$, $N = -10$ situation. Here, results from separate, 177×177 simulations are shown. Each simulation used the same initial conditions at $t = 0.18$ (generated with 177×177 spatial modes). Time steps of 1.25 and 2.5×10^{-6} were used. The solid lines are associated with the smaller time step prediction (the lines are actually small, intersecting solid points) while the open symbols are selected $\overline{Sh}$ and $\overline{Nu}$ values associated with the large time step prediction. As evident, no qualitative difference in the instantaneous $\overline{Sh}$ values can be noted. Maximum differences in instantaneous transport rates are well below 0.001% for the two time step predictions. Although no high frequency behavior is noted by visual inspection of the $\overline{Nu}$ history shown in Fig. A1 (d), careful analysis shows that $\overline{Nu}$ oscillates at the same frequency as $\overline{Sh}$, but the amplitudes of heat transfer fluctuation are extremely small due to the extremely large Lewis number of the liquid.